

# Investigated a PLL surface-modified Nylon 11 electrospun as a highly tribo-positive frictional layer to enhance output performance of triboelectric nanogenerators and self-powered wearable sensors

Gajula Prasad<sup>a</sup>, Sontyana Adonijah Graham<sup>b</sup>, Jae Su Yu<sup>b</sup>, Hongdoo Kim<sup>c</sup>, Dong-Weon Lee<sup>a,d,\*</sup>

<sup>a</sup> MEMS and Nanotechnology Laboratory, Department of Mechanical Engineering, Chonnam National University, Gwangju 61186, South Korea

<sup>b</sup> Institute for Wearable Convergence Electronics, Department of Electronic Engineering, Kyung Hee University, Yongin 17104, South Korea

<sup>c</sup> Department of Advanced Materials Engineering for Information and Electronics, Kyung Hee University, Yongin 17104, South Korea

<sup>d</sup> Center for Next-generation Research and Development, Chonnam National University, Gwangju 61186, South Korea

## ARTICLE INFO

### Keywords:

Poly-L-lysine (PLL)  
Nylon 11 electrospun  
Surface modification  
Positive polarity  
Shape adaptability  
Wearable electronics

## ABSTRACT

Although the development of self-powered triboelectric sensors (TES) is growing very rapidly, fabricating ultra-flexible, highly sensitive, lightweight and energy-sustained TES remains a tremendous challenge. Here, we report a facile poly-L-lysine (PLL) post-surface-modification technique to enhance the positive polarity of Nylon 11 electrospun membranes for the first time. Ecoflex was used as the tribo-negative layer of the triboelectric nanogenerator (TENG). The effect of the Nylon 11 electrospun membrane with PLL modification (PNy11) used as the positive layer was compared with the experimental results of the membrane without PLL modification (Ny11). The triboelectric output performances of open circuit potential and short circuit current significantly increased by more than five times (from 26 to 137 V) and four times (from 0.8 to 3.4  $\mu$ A) for PNy 11. Further, various dielectric materials (MXene and SrTiO<sub>3</sub> with different wt%) were incorporated into the Ecoflex counter layer to minimize the triboelectric loss and enhance the triboelectric performance. The 10 wt% SrTiO<sub>3</sub>-embedded Ecoflex (EC10S) and PNy 11 pair showed maximum triboelectric performance (270 V and 7.2  $\mu$ A) at a working load of 8.5 N than others. The optimized EC10S+PNy 11 TENG showed a power density of 2 Wm<sup>-2</sup>, which is sufficient to operate low-power electronics. Furthermore, the proposed EC10S+PNy 11 wearable triboelectric sensor (without spacer) exhibits high shape adaptability with a sensitivity of 9 V.Pa<sup>-1</sup> due to the imported micro-nano hierarchical roughness on the frictional layers. The proposed idea with excellent performance is expected to show great potential for use in the field of wearable electronics.

## 1. Introduction

The use of portable electronics is burgeoning day by day in consonance with the fast-growing intelligence of humans [1–6]. These portable electronics require an uninterrupted supply of electrical energy. Energy storage systems such as conventional batteries and super-capacitors are capable of operating portable electronics. However, they have limitations, such as replacing the batteries at the right time, and the lead present in these batteries is harmful to the environment. To address these challenges, a few research groups have developed self-powered electronic devices based on piezoelectric [7–9], pyroelectric [10,11], thermoelectric [12,13], electromagnetic [14], and triboelectric nanogenerators [15–18]. In recent years, self-powered flexible wearable

sensors have accelerated the ever-increasing demand for human interactive applications such as artificial e-skin and health monitoring (respiration, heartbeat, blood pressure, pulse rate, and temperature) robotics [19–23]. Wearable devices are also used as energy harvesting applications by simply converting low-frequency human-generated mechanical energy (body movements) to electrical energy [24,25]. Compared with other devices, triboelectric nanogenerators (TENGs) have gained significant attention owing to their easy fabrication, cost-effectiveness, vast materials selection, lightweight, high efficiency even at low frequency, and multi-functional modes.

TENG is a modern energy technology that can convert abundant ambient mechanical energies into electricity in the range of microwatt to milliwatt [26,27]. TENG-based systems can efficiently harvest

\* Corresponding author at: MEMS and Nanotechnology Laboratory, Department of Mechanical Engineering, Chonnam National University, Gwangju 61186, South Korea.

E-mail address: [mems@jnu.ac.kr](mailto:mems@jnu.ac.kr) (D.-W. Lee).

<https://doi.org/10.1016/j.nanoen.2023.108178>

Received 12 October 2022; Received in revised form 16 December 2022; Accepted 5 January 2023

Available online 9 January 2023

2211-2855/© 2023 Published by Elsevier Ltd.

substantial renewable energies such as vibration [28], rain [29], wind [30], and ocean energies [26], which can accompany the current energy technologies to curtail the negative environmental impact of fossil fuels [31]. Benefiting from the high sensing performance even at low frequency, small-scale human biomechanical energy harvesting, TENG, has been proposed as a pervasive energy solution for the future low-power portable and wearable electronics [32,33]. The precise material selection with a large electron affinity variance (based on triboelectric series) is the crucial factor in achieving the maximal electrical performance of TENGs [34]. For instance, TENG employing the foremost tribo-positive material and lowermost tribo-negative material exhibits supreme electrical performance. Furthermore, the performance of the device can be enhanced by altering the surface of the triboelectric layers by employing physical, chemical, biological, and hybrid modifications [35]. The physical modifications are classified as additive and non-additive surface modifications. Non-additive physical modifications include lithography, micro-nano templating, laser printing, charge injection, and plasma treatment [36–40]. These modifications can significantly increase the surface area of the frictional layers, thus increasing contact electrification and leading to high performance. Similarly, some dielectric additives such as 0D nanoparticles ( $\text{SiO}_2$ ,  $\text{TiO}_2$ ,  $\text{BaTiO}_3$ , and  $\text{SrTiO}_3$ ) [41], 1D nanowires (Ag, Gold, and ZnO) [42,43], and 2D nanoflakes (GO, CNTs, and MXene) [44,45] also enhance the dielectric constant of the tribo-layers; as a result, the TENG performance improves. In conjugation with physical modifications, chemical modifications such as UV irradiation, electroplating, electrospinning, spin coating, and self-assembly by electron-donating (amino) or electron-accepting groups (halogen) also enhance the performance of TENGs [46–53]. However, compared with individual modifications, the hybrid (more than one physical or chemical) modifications give better results [51,52].

Until now, lots of wearable electronics have been introduced into our lifestyle, including wristwatches, eyeglasses, clothes, and even smart sensors. Nevertheless, the above-mentioned devices often employ batteries as a power source, which perturb the devices' pinned flexibility, air permeability, and lightweight. On the contrary, smart tactile sensors are key for human-interactive interfaces. Even artificial skin-based sensors have the benefits of high sensitivity and shape-adaptability, but require some research on skin-friendliness and comfort. To address these challenges, flexible E-textile-based triboelectric sensors emerged to detect human motion activities. Nylon is a commonly used textile material and a prominent tribo-positive material. A few reports are available on enhancing the triboelectric performance of Nylon based fibers (using different fabrication techniques) by varying the frictional materials, as shown in [Supporting Information Table S1](#). However, the triboelectric performance especially the power density of pristine Nylon based fibers reported to date is only in the range of a few microwatts to Milli watts only to date (Dong et al. reported a maximum power density of  $7.5/\text{m}^2$ ). To further enhance the tribo positivity of Nylon membranes, in recent years, researchers fortified a new class of Nylon composite (ZnO NWs, poly-DADMC, and  $\text{AgSbS}_2$  NFs) electrospun materials, as shown in [supporting Table S2](#). Although Nylon composite electrospun membranes exhibit better triboelectric output performances, there have certain limitations: such as (i) cost and time consumption (fabrication of ZnO NWs or  $\text{AgSbS}_2$  NFs) moreover, the electrospinning of composite Nylon fibers is not an easy task for scaling. (ii) During the composite membrane fabrication, there is a possibility of sedimentation of fillers (due to the high density), which interrupts (needle blockage) the electrospinning process. (iii) The incorporation of nanofillers into the fibers decrease the flexibility; Rana et al. noticed that the elongation property of the composites decreases by almost 35% compared with that of pristine Nylon electrospun [52]. By addressing these limitations in the present study, we investigated a novel and facile post-surface modification (PLL) technique to enhance the positive polarity of Nylon 11 electrospun membranes. To the best of our knowledge, this is the first attempt to enhance the tribo-positivity of the Nylon 11 electrospun by PLL surface modification. This technique is a simple and easy fabrication, which can

be scalable, and cost-effective than the existing nylon composite techniques.

The present research mainly focused on the enhancement of triboelectric performance using innovative hybrid surface modification techniques. The tribo-positive Nylon 11 films were fabricated by the traditional electrospinning technique followed by facile poly-L-lysine (PLL) chemical modification. Similarly, the tribo-negative Ecoflex films were fabricated by combinative effects of surface templating (sandpaper) and dielectric dopants (MXene/ $\text{SrTiO}_3$ ). The as-prepared tribo films were characterized using XRD, FTIR, XPS, FESM, and EDS techniques. The TENG device was fabricated with different combinations of tribo pairs, and its triboelectric performance was evaluated in terms of  $V_{OC}$ ,  $I_{SC}$ , and charge (Q). The optimized samples were used to fabricate devices with and without a spacer for energy and wearable applications. Finally, the optimized device was used to successfully operate low-power electronics (stopwatch), LEDs lighting, and wearable applications for real-time human motion detection and differentiation.

## 2. Experimental section

### 2.1. Materials

The chemicals Nylon 11 pellets, 0.1% poly-L-lysine (PLL) solution, and  $\text{SrTiO}_3$  and solvents dichloromethane and formic acid were procured from Sigma Aldrich. MXene titanium carbide ( $\text{Ti}_3\text{C}_2\text{Tx}$ ) was purchased from Intelligent Materials Pvt. Ltd, India. Ecoflex-50 was purchased from Smooth-on, Inc (Macungie, USA), sandpaper (P-60) was purchased from Paco (South Korea), and Ni-Cu-coated polyester fabric electrodes were purchased from Solueta Co. Ltd, Korea.

### 2.2. Fabrication of Nylon-11 electrospun membrane (Ny 11)

First, a 10 wt% Nylon-11 solution was prepared by dissolving Nylon 11 pellets (1 g) in a mixture of formic acid and dichloromethane (5 mL /5 mL) with constant magnetic stirring at a speed of 350 rpm for 4 h at  $40^\circ\text{C}$ . The resulting clear solution was transferred into a 10 mL plastic syringe containing a metallic needle with an inner diameter of 0.6 mm. Electrospinning was carried out by employing a high voltage of 18 kV between the spinneret and the collector. During the spinning, a constant flow rate of 0.5 mL/h, collector rotation speed of 80 rpm, and tip-to-collector distance of 10 cm were maintained. After the spinning, the Nylon 11 fibers were collected and dried in a hot-air oven for 8 h at  $60^\circ\text{C}$  to extricate leftover solvents and stored carefully for further studies; the film was labeled "Ny 11" for further studies. The thickness of the electrospun Nylon 11 film was measured at five different positions using a thickness gauge; the average value was  $110 \pm 5 \mu\text{m}$ .

### 2.3. PLL surface modification of Nylon-11 electrospun membrane (PNy 11)

To enhance the tribo-positive polarity of Nylon-11, electron-donating amino groups containing PLL solution were used. Before modification, the electrospun Nylon membranes were subjected to oxygen plasma with a power of 80 W for 1 min to concoct hydroxyl groups (-OH) over the Nylon electrospun surface. Then, aqueous PLL solution was spin-coated onto the pretreated Nylon surface with the following spinning parameters: low speed of 500 rpm for 5 s followed by a high-speed of 1000 rpm for 30 s. The hydroxyl groups (-OH) present on the Nylon surface form hydro bonds with the  $-\text{NH}_2$  group in the PLL solution [49]. Finally, the PLL-modified Nylon electrospun membranes were dried in a hot-air oven at  $40^\circ\text{C}$  for 8 h. After PLL modification, the film was named "PNy 11" for further studies. The overall schematic representation of electrospinning and surface modification is shown in [Fig. 1](#) (a). The optical images of electrospun membranes before and after PLL medication are shown in [Supporting information Fig. S1](#) (a and b).

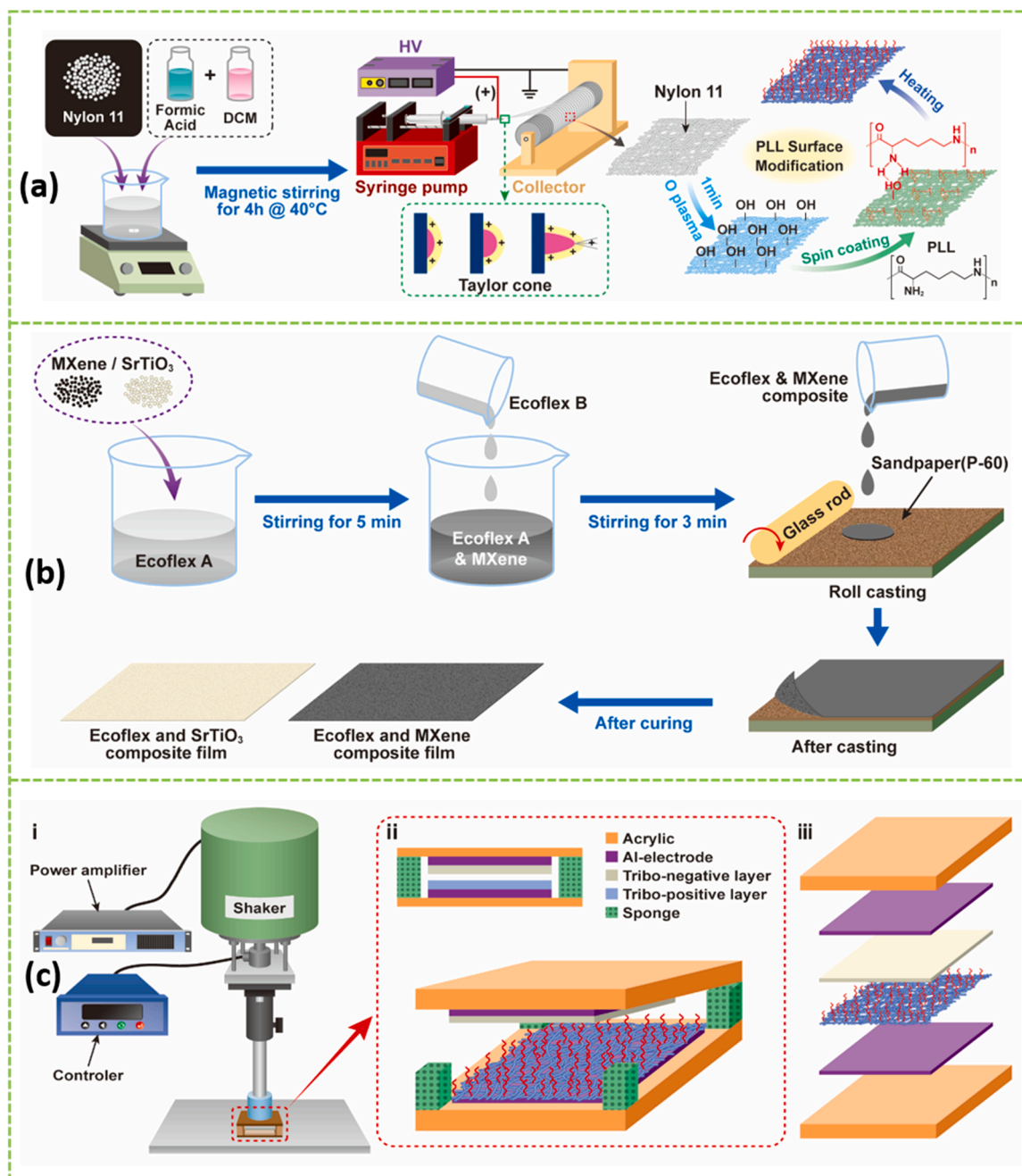


**Fig. 1.** (a) Schematic illustration of electrospinning of Nylon 11 followed by PLL surface modification. (b) Schematic illustration of Ecoflex and its composite (MXene and SrTiO<sub>3</sub>) casting process. (c) (i) TENG measurement setup, (ii) TENG device with spacer, and (iii) device cross-sectional view.

#### 2.4. Fabrication of micro-structured Ecoflex and its composite films

Pristine Ecoflex films (EC) were fabricated by the facile casting of pre-mixed Ecoflex- A and B (1/1, w/w) on rough sandpaper (grit 60). Whereas Ecoflex composite films (MXene and SrTiO<sub>3</sub>) with different wt % 3, 5, and 10 were fabricated using additives pre-mixed Ecoflex A instead of Ecoflex A, and the rest of the process was similar. All casted films were cured for 24 h at ambient conditions. After curing, the films were carefully removed from the sandpaper and stored in a desiccator for further use. The Ecoflex and the composite coatings with different wt % (3, 5, and 10) of MXene and SrTiO<sub>3</sub> were named EC3M, EC5M, and EC10M and EC3S, EC5S, and EC10S, respectively. The thickness of all casted films was measured at five different locations, and the average value was in the range of  $220\text{--}290 \pm 10 \mu\text{m}$ . A complete schematic

representation of the Ecoflex composite film fabrication is shown in Fig. 1(b). The transparent Ecoflex films (EC) turned black when MXene was added (EC3M, EC5M, and EC10M), whereas they turned into a cream color upon adding SrTiO<sub>3</sub> (EC3S, EC5S, and EC10S). The optical images for fabrication and cast films (different wt%) are shown in Fig. S2 in the Supporting Information.

#### 2.5. Device fabrication

##### 2.5.1. Fabrication of TENG device with a spacer

The triboelectric devices were fabricated with different combinations of tribo-positive (Ny 11 and PNY 11) and tribo-negative (EC, EC3M, EC5M, EC10M, EC3S, EC5S, and EC10S) layers. Initially, both tribo layers were cut into  $2.1 \times 2.1 \text{ cm}^2$  pieces and then stuck on one



side of adhesive  $2 \times 2 \text{ cm}^2$  Al electrodes. The slightly sized tribo films protect the interference of the top and bottom electrodes. Finally, both films were aligned exactly opposite to each other with a spacing of 2 mm (using a sponge). The cross-sectional view of the device is shown in Fig. 1(c)(ii) and (iii), and the optical images of the device are shown in Fig. S3 in the Supporting Information.

### 2.5.2. Fabrication of triboelectric sensor (TES) without spacer

Similarly, the TES devices of various sizes ( $2 \times 2 \text{ cm}^2$  and  $8 \times 2 \text{ cm}^2$ )

were fabricated without any spacer. Here, the only change was that Ni-Cu-coated fabric electrodes were used (to attain flexibility) instead of the Al electrode, followed by encapsulation with PET films. The PET film encapsulation protects the device from the surrounding noise and humidity. Optical images of the devices are shown in Fig. S4 in the Supporting Information.

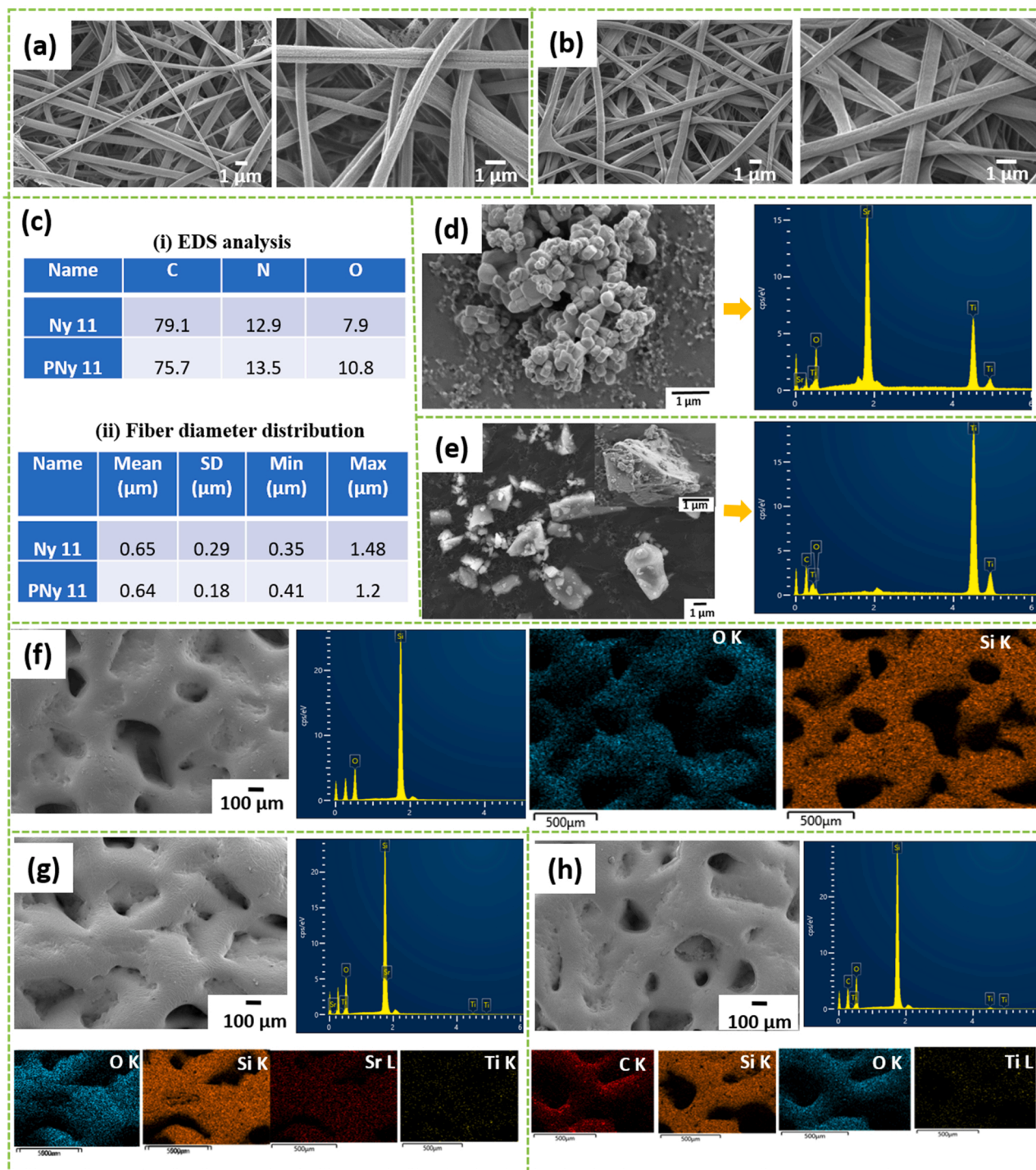


**Fig. 2.** (a) Surface morphology of Ny 11. (b) Surface morphology of PNY 11. (c) (i) Comparison of EDS analysis and (ii) fiber diameter distribution of Nylon 11 before and after surface modification. (d) and (e) surface morphology and EDS analysis of as-received  $\text{SrTiO}_3$  and MXene powders, respectively. (f), (g), and (h) surface morphology, EDS, and elemental mapping of EC, EC10S, and EC10M, respectively.



## 2.6. Characterization

The surface morphology and elemental composition of the as-prepared tribo layers were examined by FE-SEM (JEOL, JSF7900F) at an acceleration of 2 kV and EDS (Oxford instruments, Ultim Max) techniques. Before SEM analysis, the as-prepared films were subjected to platinum sputtering with operational parameters of 90 s at 0.1 mA current. Further, the phase purity of the as-prepared films was examined through the XRD pattern (PANalytical X'Pert Pro) by employing  $\text{CuK}\alpha$  irradiation; the scanning range of  $2\theta$  values was  $5\text{--}90^\circ$ , and the scanning speed was  $8.5^\circ \text{ min}^{-1}$ . The chemical changes in Nylon 11 before and after the surface modifications were analyzed by Fourier transform infrared (FTIR) spectrometer (PIKE technologies, Spectrum 3 FT-IR). The measurements were carried out in an attenuated total reflection (ATR) mode with the following measuring parameters:  $4 \text{ cm}^{-1}$  resolution and 20 scans. X-ray photoelectron spectra (XPS) of the as-prepared Nylon 11 electrospun and PLL surface-modified Nylon 11 were recorded with Thermo Scientific, K alpha+ surface analyzer, using non-monochromatic  $\text{AlK}\alpha$  radiation ( $1486.6 \text{ eV}$ ) as the X-ray source. The survey spectra were obtained in the digital mode interconnected to PC with 200 eV pass energy hemispheres of the electron analyzer and a step increment of 0.1 eV. Similarly, the core-shell spectrums (C1s, N1s, and O1s) were recorded with a pass energy of 50 eV and step increment of 0.1 eV. The electrical output such as open circuit potential ( $V_{\text{OC}}$ ) was measured using an oscilloscope (DP04104, Tektronix), which integrated with high voltage probe (P5100A) having input impedance of  $40 \text{ M}\Omega$ . Short circuit current ( $I_{\text{SC}}$ ), and charge (Q) measured by an electrometer (Keithley 6514). A custom-made dynamic shaker (see Fig. 1(c) (i)) employed periodic external loads during the electrical measurements. The human motion monitoring studies were carried out using the BIO-PAC MP 150 data acquisition system (BIOPAC Systems, Inc., USA) with an integration piezo amplifier (conditions:  $R_{\text{in}}$  of  $100 \text{ M}\Omega$  and gain of 0 dB), and the data were saved wirelessly in the PC using acknowledgment 4.2 software.

## 3. Results and discussion

The surface morphology and elemental analysis of the as-prepared tribo-layers and commercially procured  $\text{SrTiO}_3$  and MXene powders were examined using FE-SEM and EDS analysis. The surface morphology of electrospun Nylon 11 shows the formation of neat fibers without beads, implying that the electrospinning parameters were optimal. Further, the fiber diameter was calculated using ImageJ software; initially, the diameters of 20 individual fibers were calculated, and the average was taken, as shown in Table S3 in the Supporting Information. The average diameter of the fiber was approximately 650 nm, and they were randomly oriented, as shown in Fig. 2(a). The random orientation of the fibers in the membrane is attributed to the low collector speed (80 rpm). The uneven nonwoven polymer surfaces are preferred in TENG (it will act as a pseudo-spacer); hence, regular arrangements are not considered. Each fiber exhibits a rough nodular morphology, which can be observed in the magnified SEM images, as shown in Fig. S1(a') in the Supporting Information. Similarly, the surface morphology was examined after the PLL surface modification; no significant changes were observed except that the fiber becomes smoother, as shown in Fig. 2b and Fig. S1(b') in the Supporting Information. This could be attributed to the spin coating step in which the PLL solution accumulates over the Nylon fibers. For better comprehension of the surface modification phenomenon, before (Ny 11) and after (PNy 11) surface-modified samples were examined by EDS spectroscopy. Unfortunately, both Nylon and PLL have similar atoms (C, N, and O) in their chemical structure, and hence it is hard to distinguish precise changes. However, there was a slight increment in the atomic wt% of O (from 7.9 to 10.8) and N (from 12.9 to 13.5) after surface modifications, as shown in the inset table in Fig. 2(c). The change in the morphology and elemental composition is the primary evidence of the surface modification of the

Nylon 11 electrospun membrane, which is further proven through XPS, XRD, and FT-IR studies.

The surface morphology of  $\text{SrTiO}_3$  powder shows a cubic shape with irregular sizes, as shown in Fig. 2(d), and the maximum size was less than a micron. The MXene powder shows sheets-like (2D) structures with an average size of  $2\text{--}3 \mu\text{m}$ , as shown in Fig. 2(e). The EDS results confirm the presence of characteristic elements of Sr, Ti, and O for  $\text{SrTiO}_3$  and C, O, and Ti for MXene, as shown in Fig. 2(d) and (e). The EC and its composite cast films show similar morphologies with deep valleys and hills that resemble the sandpaper texture shown in Fig. 2(f-h) and Fig. (S5 and S6) in the Supporting Information. The elemental analysis shows the existence of characteristic elements of Sr and Ti for  $\text{SrTiO}_3$  and Ti and C for MXene composites, and the elemental mapping shows the uniform distribution of  $\text{SrTiO}_3$  and MXene powders. When the  $\text{SrTiO}_3$  and MXene contents increase from 3 to 10 wt%, the corresponding elemental compositions also increase. However, in the case of EC and  $\text{SrTiO}_3$  composites, the distinction between Si and Sr is challenging because the binding energies of Si and Sr are similar range. To determine the exact Sr distribution, we voluntarily removed the Si element, and the results are shown in Fig. S7 in the Supporting Information.

To further understand the surface modifications, the Ny 11 and PNy 11 films were systematically studied using XRD, FTIR, and XPS. No significant differences were observed in the XRD patterns of the samples before and after surface modifications. A single broad peak was observed at a  $2\theta$  value of  $21.4^\circ$ , which corresponds to C, attributed to both Nylon and PLL, as shown in Fig. 3(a). This result confirms that the PLL surface modification does not affect the crystallinity of Nylon 11. The FTIR spectra of Ny 11 electrospun show the characteristic vibrations of polyamide 11 at  $3277 \text{ cm}^{-1}$  (N-H bond),  $3071 \text{ cm}^{-1}$  (Amide II, N-H, resonance),  $1634 \text{ cm}^{-1}$  (Amide I, C=O stretch),  $1471 \text{ cm}^{-1}$  (C=O, bending), and  $717 \text{ cm}^{-1}$  ( $\text{CH}_2$  rocking) [54]. These results confirm the formation of Nylon 11 electrospun fibers. After PLL modification, no significant changes were observed in the surface morphology except the fiber smoothness, as shown in Fig. 3(b). Furthermore, the chemical changes after the modifications of the Ny 11 sample were analyzed by XPS spectroscopy, and the survey spectrum indicates that there were no significant peak changes in C1s, N1s, and O1s, as shown in Fig. 3(c). However, after the surface modification, the O1s peaks were slightly broadened with higher intensity than unmodified Ny 11. For further clarity, casa XPS curve fitting was performed for the core-shell spectra of C1s, N1s, and O1s, as shown in Fig. 3(c) and Fig. S8 in the Supporting Information. The core-shell spectrum of O1s before modification consists of only two peaks, at 531.3 eV and 532.7 eV, which represent the characteristic peaks of N-C=O and C(C=O)-OH, respectively [54]. After PLL modification, an additional peak at 533.5 eV can be observed, which represents the O=C-OH bonding. This is mainly attributed to the formation of inter-hydrogen bonding between the  $\text{-NH}_2$  group from PLL and O from Nylon. The C1s core-shell spectrum before modification contains three major peaks at 284.4 eV, 285.6 eV, and 287.6 eV representing C-C, C=O, and N-C=O bonds, respectively [54]. After modification, the additional tiny peak observed at 288.7 eV corresponds to the =C-OH bond formation during the plasma treatment or the formation of hydro bonding between the -OH groups of Nylon 11 surface and  $\text{-NH}_2$  groups of PLL [49]; the changes are shown in Fig. 3(c). The nitrogen core-shell peaks remain unchanged after surface modification (shown in Fig. S8 in the Supporting Information). These results confirm that the PLL coating only forms inter-hydrogen bonding with the Nylon surface.

Fig. 3(d) and (e) show the XRD pattern of Ecoflex and its composite cast films. Fig. 3(d) shows the diffraction peaks of the as-received  $\text{SrTiO}_3$  powder at the  $2\theta$  values of  $22.7^\circ$ ,  $32.4^\circ$ ,  $39.9^\circ$ ,  $46.5^\circ$ ,  $52.3^\circ$ ,  $57.7^\circ$ ,  $67.9^\circ$ ,  $72.6^\circ$ , and  $77.2^\circ$  corresponding to the (100), (110), (111), (200), (210), (211), (220), (300), and (310) reflections, respectively. The  $\text{SrTiO}_3$  XRD peaks coincide well with the JCPDS card number 35-0734, which conforms to the as-received powder as a simple cubic crystalline structure. Similarly, the XRD pattern of pristine Ecoflex cast film shows a single

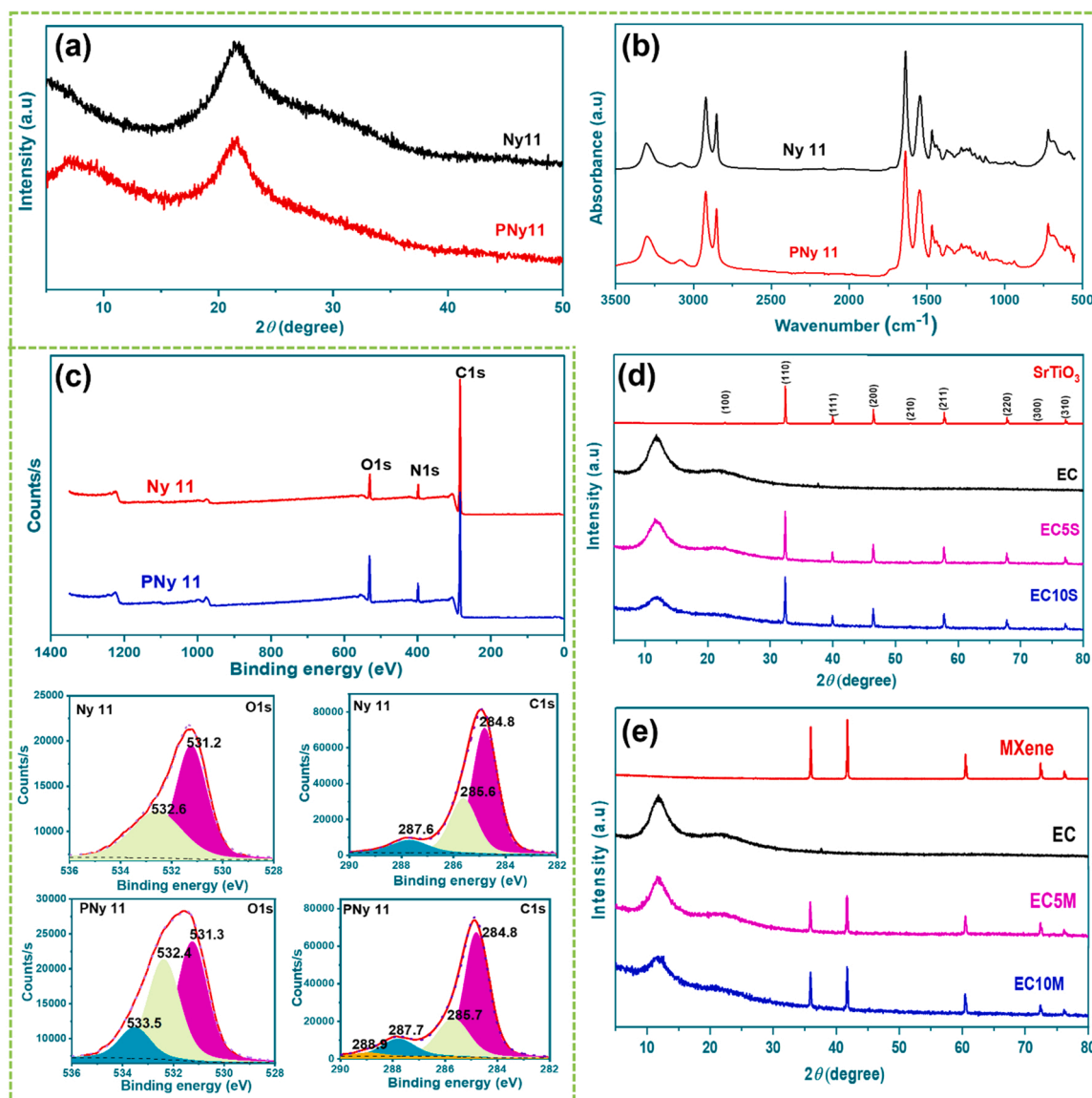


**Fig. 3.** (a) XRD pattern and (b) FTIR spectroscopic studies of Nylon 11 electrospun before and after surface modification. (c) XPS survey spectra and core-shell spectra of Nylon 11 electrospun before and after modification. (d) and (e) XRD pattern of Ecoflex and its composites with SrTiO<sub>3</sub> and MXene films, respectively.

broad peak at the  $2\theta$  value of  $11.6^\circ$ . The XRD pattern of the composite films EC5S and EC10S shows the co-existence of SrTiO<sub>3</sub> and Ecoflex peaks, as shown in Fig. 3(d). When the SrTiO<sub>3</sub> content increases from 5 to 10 wt%, the peak intensity at  $11.6^\circ$  (Ecoflex) decreases slightly and a corresponding increase is observed in the peak intensity at  $32.4^\circ$  (SrTiO<sub>3</sub>). Similarly, Ecoflex and MXene peaks coexist in the XRD pattern of the EC5M and EC10M composites, as shown in Fig. 3(e). The above-mentioned results confirm the formation of Ecoflex composite films.

### 3.1. Optimization of TENG (with spacer) device and its energy harvesting applications

#### 3.1.1. Working principle

The TENG device fabricated in this study is based on a contact separation mechanism, for instance, we consider the EC10S+PNy 11 with a spacer to explain the working mechanism, as shown in Fig. 4(a). Here, the EC10S film acts as a tribo-negative layer, whereas the PNY 11 film acts as a tribo-positive layer. Before applying external pressure, the two films are separated from each other and exhibit neutral charges, as shown in step (i). On applying the external force, the top EC10S layer

comes in contact with the bottom PNY 11 layer. According to the triboelectric principle, equal and opposite charges are generated on contact layers, based on their electron affinities. Compared with EC10S, PNY 11 has a higher tendency to lose electrons; hence, it gets positively charged and the counter EC10S film gets negatively charged. Owing to the electric equilibrium, there is no current flow in step (ii). When you start releasing the external load, the films slowly move away from each other, and a potential difference is created between the electrodes. As a result, the electrons move from the top to the bottom electrode to balance the potential differences in step (iii). This process continues until the electrodes and the corresponding tribo-films attain an equal number of opposite charges owing to the electrostatic induction, as shown in step (iv). On further applying the external force, the electrostatic induction balance gets fragmented; therefore, the electrons flow in a reverse direction from bottom to top, as shown in step (v). This periodic cyclic contact and separation process is repeated and continuously generates alternating current (AC), as shown in Fig. 4(a) (vi).

#### 3.1.2. Optimization of triboelectric performance

The output performance ( $V_{OC}$ ,  $I_{SC}$ , and  $Q$ ) of the device with a spacer

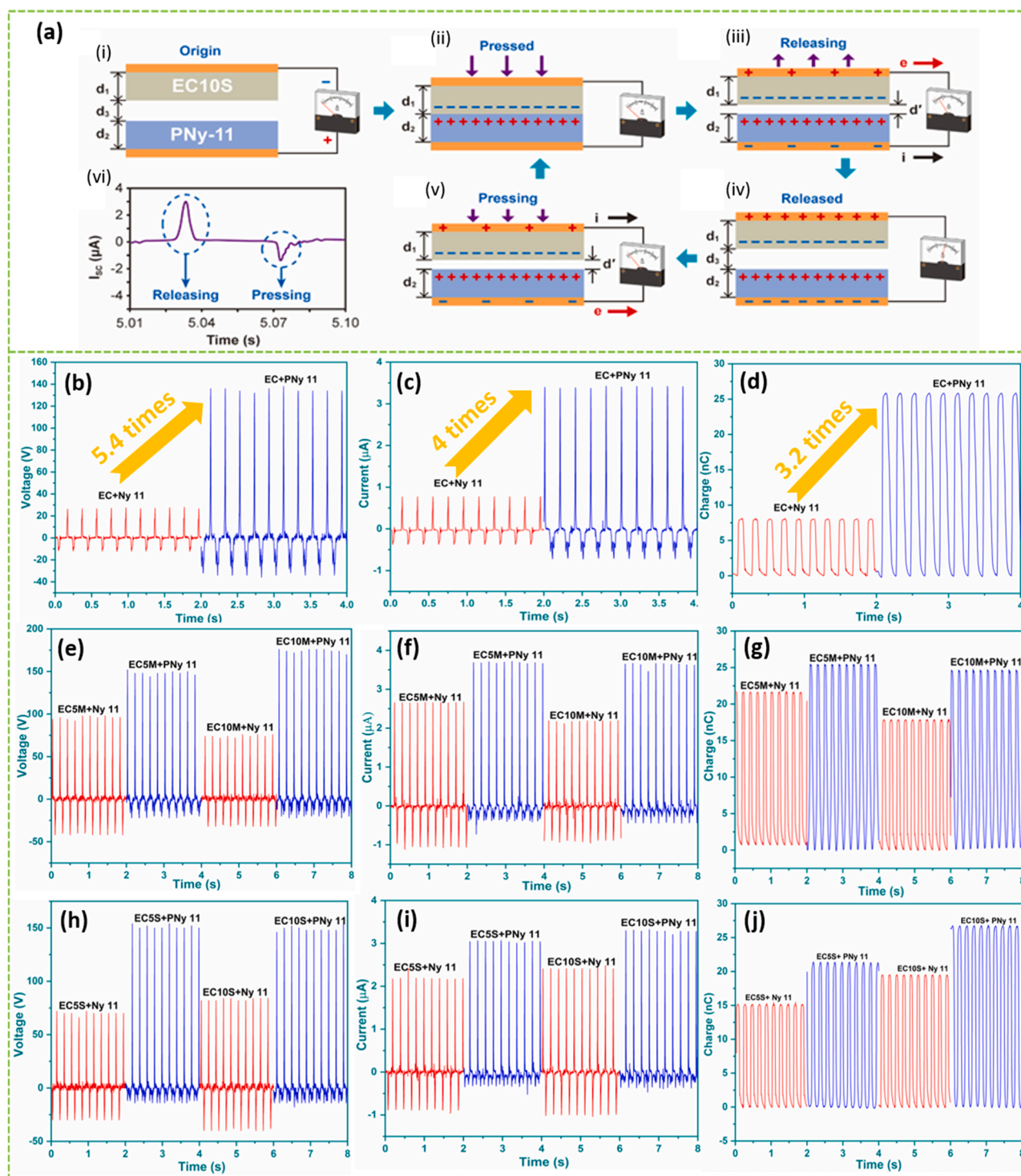


**Fig. 4.** (a) Schematic illustration of the working mechanism. TENG output performance ( $V_{OC}$ ,  $I_{SC}$ , and  $Q$ ) of Ny 11 and PNY 11 films against EC (b-d), EC5M and EC10M (e-g), and EC5S and EC10S (h-j), respectively. The above TENG measurements were carried out by employing a constant load of 4.5 N and a frequency of 5 Hz.

(2 mm) was evaluated by employing a periodic load of 4.5 N at a constant frequency of 5 Hz. The output performance ( $V_{OC}$ ,  $I_{SC}$ , and  $Q$ ) of Ny 11 and EC tribo pair was only 26 V, 0.8  $\mu A$ , and 8.1 nC, respectively, whereas PNY and EC tribo pair exhibited enhanced output performance of 137 V, 3.4  $\mu A$ , and 26 nC, respectively, as shown in Fig. 4(b-d). The enhancement of the TENG performance in terms of  $V_{OC}$ ,  $I_{SC}$ , and  $Q$  was more than five times (from 26 to 137 V), four times (from 0.8–3.4  $\mu A$ ), and three times (from 8.1 to 26 nC), which indicates the significance of

PLL modification. Here, the PLL offers more electron-donating atoms, such as N and O, which are critical for enhancing the positive polarity of Nylon [49,54]. These results indicate that PLL surface modification can be used to enhance the output performance of tribo-positive materials (Nylon 11). Although TENGs exhibit high output voltages ( $V_{OC}$ ), there is a limitation of power due to the electrically insulating nature of tribo (polymer) materials. To overcome this limitation, in this study, we incorporate MXene and  $SrTiO_3$  dielectric materials into the Ecoflex



matrix. These dielectric materials prevent triboelectric charge loss after contact electrification. Fig. 4(e-g) and Fig. S9(a-d) in the Supporting information show that when the MXene content increases from 3 wt% to 10 wt%, the output performances also gradually increase. The EC+Ny 11 tribo pair shows only 26 V, whereas the EC5M+Ny 11 combination shows almost 4 times higher performance (95 V), as shown in Fig. 4(b and e), and the maximum TENG output is almost 6.5 times higher (177 V) for the EC10M+PNy 11 pair. This could be because the embedded MXene sheets act as a pseudo-capacitor in the Ecoflex matrix and enhance the output performances until the MXene concentration

attains its threshold value [45]. Thus, both modified tribo-layers showed enhanced output performance (177 V and 3.7  $\mu$ A) than single modified ones, as shown in Fig. 4(e and f). However, the output performance ( $V_{OC}$ ,  $I_{SC}$ , and  $Q$ ) slightly decreased for EC10M when the used counter material is Ny 11, this is because when the MXene concentration increased beyond the threshold value, the dielectric constant drops because of increased connections between the Mxene sheets. Rana et al. reported similar studies with MXene concentration; beyond 10 wt%, the dielectric constant starts dropping because the Mxene sheets form connecting networks with the film [55]. Interestingly, when the PNy 11 is

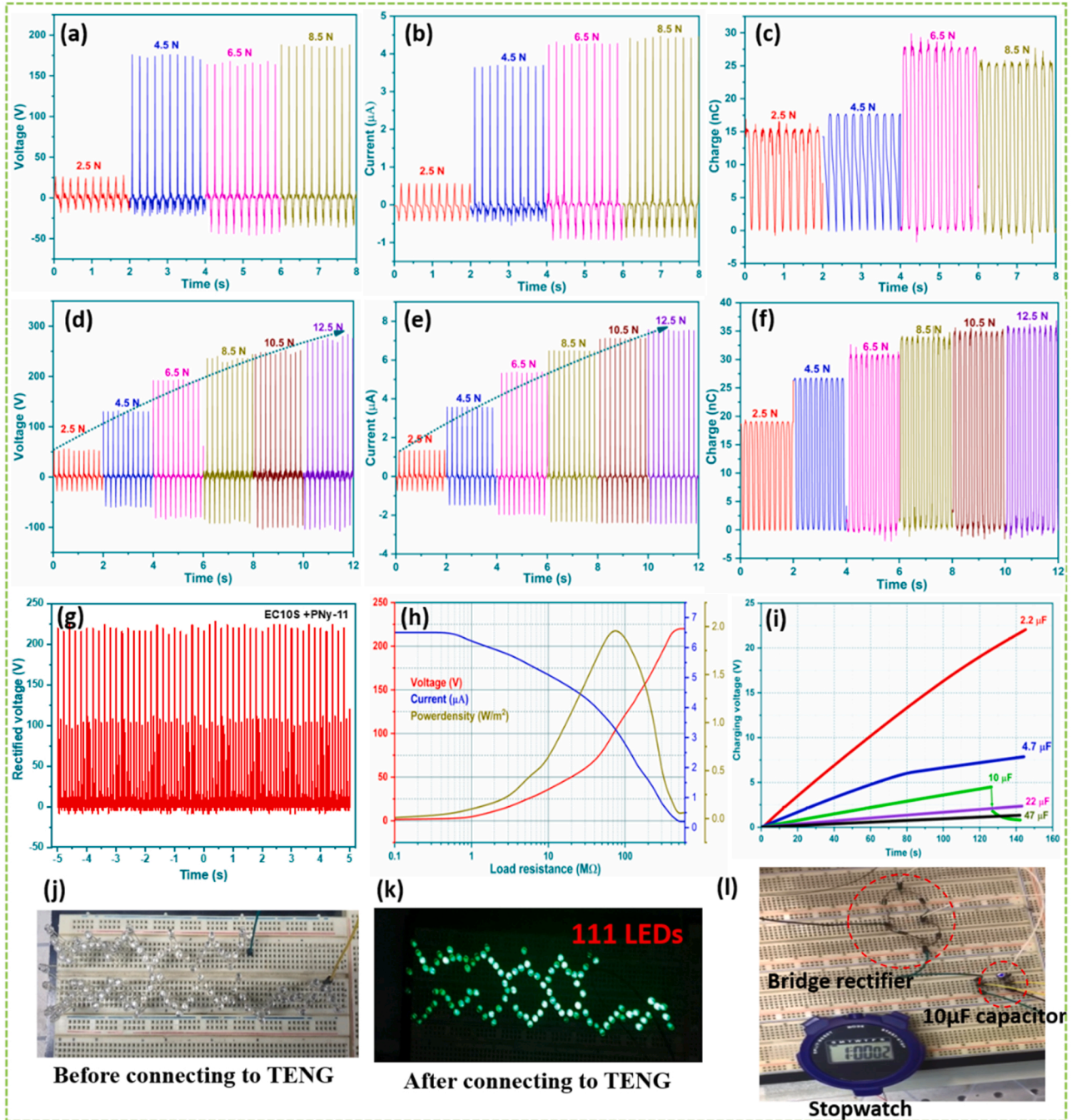


**Fig. 5.** (a-c) Output performances ( $V_{OC}$ ,  $I_{SC}$ , and  $Q$ ) of EC10M+PNy 11 TENG device as a function of load (2.5–8.5 N). (d-f) Output performances ( $V_{OC}$ ,  $I_{SC}$ , and  $Q$ ) of EC10S+PNy 11 TENG device as a function of load (2.5–12.5 N). (g) Rectified voltage of EC10S+PNy 11 TENG (h) EC10S+PNy 11 TENG output performance and power density as a function of input load resistance (100 kΩ to 600 MΩ) (i) EC10S+PNy 11 TENG device energy storage with various capacitors (2.2–47  $\mu$ F) and charging and discharging cycles using 10  $\mu$ F with a connecting stopwatch. (j) and (k) optical images of 111 LEDs before and after connecting EC10S+PNy 11 TENG. (l) Optical image of powering stopwatch setup. For results shown in (g-i), constant pressure was maintained with 8.5 N load at 5 Hz frequency.

used as a positive frictional layer, it contains more electron-donating (-N) atoms which can help to sustain higher output voltages, even though the dielectric constant of EC10M decreases. When the electron donating groups increase on the positive layer it will create a higher potential difference between the frictional layers whereas the unmodified Ny 11 has a less positive charge comparatively. Feng et al. reported the effect of PLL surface modification of dry leaves to enhance the triboelectric polarity (49). By comparing the above results with the reference studies, we believe that the PLL surface modification of Nylon 11 electrospun membranes plays a significant role in attaining high electrical output performances. On the contrary, the EC and SrTiO<sub>3</sub> composite films show a linear increment in the TENG output performance as the filler concentration increases from 3 wt% to 10 wt%, as shown in Fig. 4 (h-j) and Fig. S9(e-h) in the Supporting Information. In both cases (SrTiO<sub>3</sub> and MXene), the 10 wt% embedded Ecoflex samples show maximum output for EC10M and EC10S. The overall comparison of the triboelectric performance in terms of  $V_{OC}$  and  $I_{SC}$  before and after modification of Nylon 11 electrospun against various tribo-negative materials is shown in Fig. S10(a and b), respectively, in the Supporting Information.

Further, the optimized EC10M+PNy 11 and EC10S+PNy 11 TENG devices were evaluated as a function of load from 2.5 N to 12.5 N, and the results are shown in Fig. 5(a-f). Fig. 5(a-c) shows the  $V_{OC}$ ,  $I_{SC}$ , and  $Q$  for the EC10M+PNy 11 device when the external load increases from 2.5 N to 8.5 N at a constant frequency of 5 Hz. At a low external load (2.5 N), the device output performance (25 V, 0.5  $\mu$ A, and 15 nC) was also quite low. A sudden improvement in the performance was observed at 4.5 N (170 V, 3.6  $\mu$ A, 18 nC). The performance marginally increased up to 6.5 N and then almost saturated with maximum output  $V_{OC}$  (172 V),  $I_{SC}$  (4.2  $\mu$ A), at 8.5 N. Interestingly, the charge slightly decreased from 27 nC to 25 nC when the load increased from 6.5 to 8.5 N. This may be due to when the load reaches 8.5 N the EC10M film is more squeezed as a result the MXene sheets come close to each other within the film and leading to the formation of the connecting networks within the film. Rana et al. also explained this phenomenon when the MXene connects each other there will be a chance of leakage of charge. (55). Whereas the EC10S+PNy 11 sample showed a linear increment in the TENG performance when the load increased from 2.5 N to 12.5 N, as shown in Fig. 5(d-f). When the load increased gradually from 2.5 to 12.5 N, the TENG performance  $V_{OC}$  (from 50 to 270 V),  $I_{SC}$  (from 1.1 to 7.2  $\mu$ A), and  $Q$  (from 18 to 35 nC) also increased. This is because when the external force increases, the area of contact increases because of these increased accumulations of charges. Once the charges on the surfaces increase, the potential difference also increases, which leads to a higher output performance. Due to the limitation of our lab setup, we could not apply a load higher than 12.5 N, and based on the trend, the output performance may increase with a further increment of load. Therefore, EC10S+PNy 11 was optimized for further studies. Due to the linear relation between the external load and the output performance, the EC10S+PNy 11 TENG can be used as a force sensor. For instance, if the output performance of the device is known, we can predict the force acting on it; this has potential applications in differentiating multimode vibrations.

### 3.1.3. Energy harvesting applications

To validate the feasibility of the EC10S+PNy 11 device in real-time applications, the electric output generated by the device was connected to low-power electronic liquid crystal displays (LCD) such as a stopwatch. The voltage generated by the device was in an alternative waveform, which cannot directly operate portable electronics. Hence, before connecting to a portable electronic device, the alternative voltage generated from the devices was converted to direct voltage using a full-bridge rectifier circuit. Further, the rectified voltage was stored in a capacitor before connecting the portable electronics. Fig. 5(g) shows the rectified voltage of 220 V for the EC10S+PNy 11 device at a working load of 8.5 N and a frequency of 5 Hz. The rectified voltage was stored in

various capacitors of 2.2  $\mu$ F, 4.7  $\mu$ F, 10  $\mu$ F, 22  $\mu$ F, and 47  $\mu$ F for around 140 s and stored maximum voltage of 22 V, 7 V, 4.9 V, 2.2 V, and 1.1 V, respectively, as shown in Fig. 5(j). To demonstrate the operation of the stopwatch (battery removed as shown in Fig. S11 in the Supporting Information), initially, the capacitor (10  $\mu$ F) was charged for 125 s using the EC10S+PNy 11 device with a load of 8.5 N at 5 Hz and connected to a stopwatch. It operated for 7 s without interruption, as shown in Fig. 5 (l) and Video S1 in the Supporting Information; thus, it has the potential to operate low-power electronics. In addition, the EC10S+PNy 11 device can light up 111 LEDs without using any rectifier and capacitor with an operational load of 8.5 N at 5 Hz, as shown in Fig. 5(j and k) and Video S1 in the Supporting Information.

Supplementary material related to this article can be found online at doi:10.1016/j.nanoen.2023.108178.

Finally, the device output performance ( $V_{OC}$  and  $I_{SC}$ ) of EC10S+PNy 11 as a function of the input load resistance (100  $\Omega$  to 600 M $\Omega$ ) was evaluated, as shown in Fig. 5(h). When the input load resistance reaches 100 k $\Omega$ , there are no significant changes in  $V_{OC}$  and  $I_{SC}$ ; beyond that, the  $V_{OC}$  gradually increases and reaches a maximum at 220 V at 450 M $\Omega$ . The  $I_{SC}$  value (6.5  $\mu$ A) remains constant up to 1 M $\Omega$ ; beyond that,  $I_{SC}$  follows a reverse trend with input load resistance and becomes almost negligible at 500 M $\Omega$ , as shown in Fig. 5(h). The power density of the device was calculated using the following Eq. (1).

$$\text{Power density}(P) = \frac{I^2 R}{A} \quad (1)$$

Here,  $I$  represents the short circuit current (A),  $R$  represents the input resistance ( $\Omega$ ), and  $A$  represents the area of the electrode ( $\text{m}^2$ ). As shown in Fig. 5(h), the power density gradually increases with increasing input resistance until it reaches saturation. According to maximum power transfer theory, the maximum power is attained when the external load is equal to the internal impedance value [56]. In this study, the power density values start increasing gradually at a load of 100 k $\Omega$  and reach the maximum value of 2 W/ $\text{m}^2$  at 70 M $\Omega$ ; further increase in the load resistance decreases the power density, and it becomes almost negligible at 500 M $\Omega$ , as shown in Fig. 5(h). The TENG exhibits superior electrical performance; however, it is not suitable for detecting low vibrational human activities due to the spacer. To address this, in this study, we also fabricated triboelectric sensors without a spacer.

## 3.2. Optimization of TES (without spacer) and wearable applications

### 3.2.1. Working mechanism

The mechanism without a spacer is similar to the spacer mechanism shown in Fig. 6(a); here, the two triboelectric materials are slightly inter-curse with each other before applying external pressure, as shown in step (i). However, the two frictional materials are only partly in contact with each other, and there is some space in between them (due to the roughness of the EC10S cast film and unevenness of electrospun PNy 11). This can be explained based on the Volta-Helmholtz hypothesis—when the surface roughness of the frictional layer increases, the area of contact also increases, which enhances the surface charge [57]. According to the triboelectric series, the surface-modified nylon (PNy 11) acts as a tribo-positive layer, whereas the Ecoflex-based EC10S film acts as a tribo-negative layer. When an external load is applied (either tapping, twisting, or bending), the two tribo films squeeze together and make maximum contact as shown in step (ii). As a result, more charges are created at the interface of the material. When the load is removed slowly the two films are partly separated and voltage differences will create among the electrodes and the electrons will flow from the top electrode to the bottom and get a positive signal as shown in step (iii). This process will continue until the equilibrium state is shown in (iv). When the periodic force is applied again (v) the electrons start flowing back from the bottom to the top to create an electrically balanced which gives the negative signal. This cyclic process is repeated several times



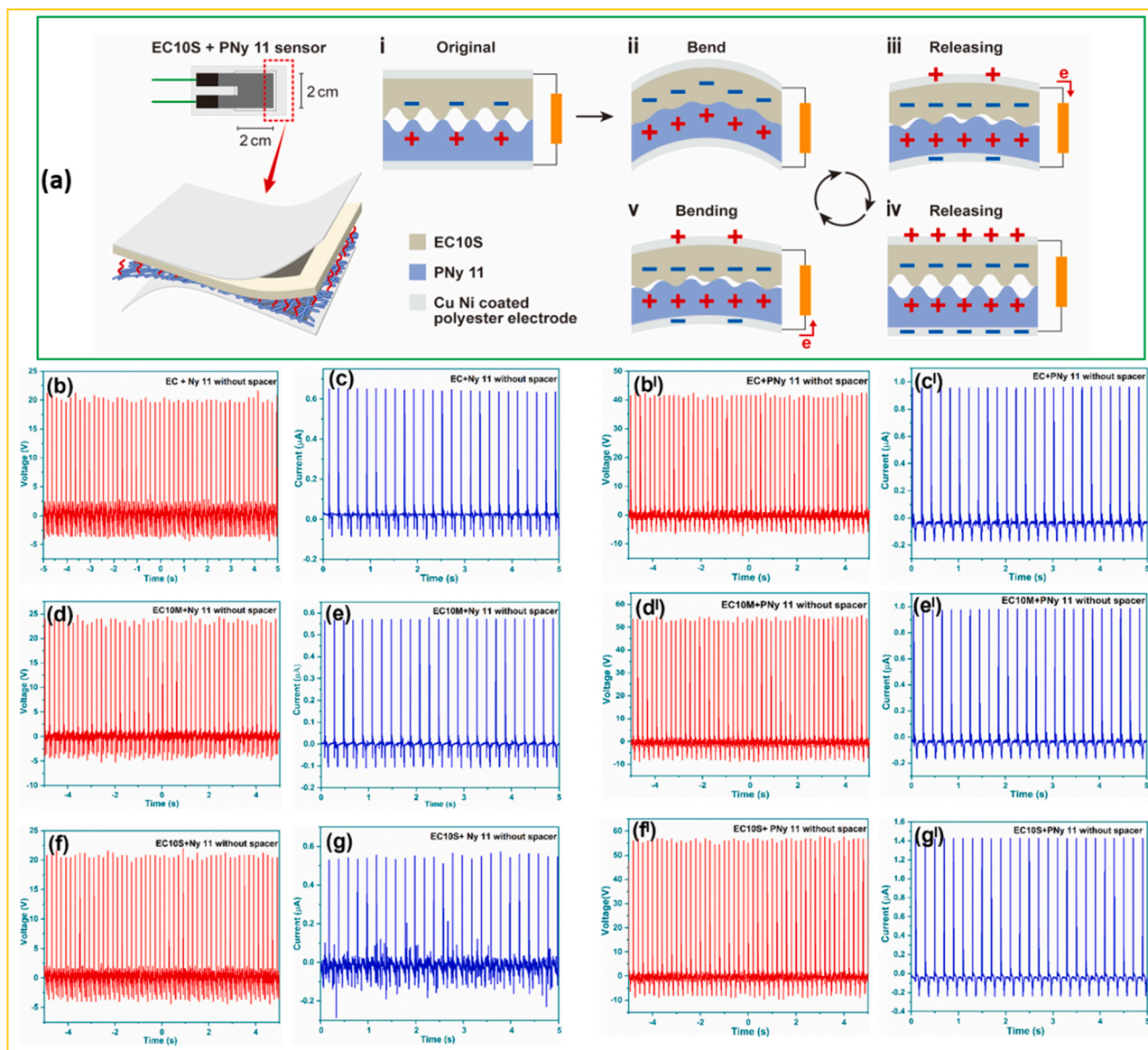


**Fig. 6.** (a) Schematic illustration of triboelectric sensor fabrication and its cross-section view and working mechanism. (b, c) and (b', c') show the triboelectric performance ( $V_{OC}$  and  $I_{SC}$ ) of EC against Ny 11 and PNy 11, respectively. (d, e) and (d', e') show the triboelectric performance ( $V_{OC}$  and  $I_{SC}$ ) of EC10M against Ny 11 and PNy 11, respectively. (f, g) and (f', g') show the triboelectric performance ( $V_{OC}$  and  $I_{SC}$ ) of EC10S cast film against Ny 11 and PNy 11, respectively. During the electrical measurements, a constant load of 6 N at 5 Hz frequency was maintained.

during the measurement, and a continuous alternative current form is produced.

### 3.2.2. Optimization of triboelectric performance

The TES ( $2 \times 2 \text{ cm}^2$ ) without a spacer is fabricated by varying different combinations of tribo-positive (Ny 11 and PNy 11) and tribo-negative (EC, EC10M, and EC10S) frictional layers; the results are shown in Fig. 6. The cross-sectional view of TES is shown in Fig. 6(a). The output performance ( $V_{OC}$  and  $I_{SC}$ ) of the EC and Ny 11 tribo pair shows only 20 V and  $0.7 \mu\text{A}$ , respectively, as shown in Fig. 6(b and c), whereas the EC and PNy 11 pair exhibit approximately 40 V and  $0.9 \mu\text{A}$ , respectively, as shown in Fig. 6(b' and c'). The voltage was almost two times higher for surface-modified samples, whereas the same tribo pair exhibited more than five times higher voltage with a spacer. The EC10M and EC10S tribo negative films produce output performance of 24 V and  $0.5 \mu\text{A}$  and 21 V and  $0.5 \mu\text{A}$  against the Ny 11 sample, respectively, as shown in Fig. 6(d-g). In contrast, the EC10M and EC10S tribo negative films produce output performance of 54 V and  $0.9 \mu\text{A}$  and 56 V and

$1.4 \mu\text{A}$  against the PNy 11 sample, respectively, as Fig. 6(d'-g'). The combination of surface modification and dielectric dopant layers results in a significantly enhanced output performance as compared with that of the individual ones. Among the combinations, the EC10S+PNy 11 sample shows the best performance; hence, it is optimized for further wearable sensor applications.

### 3.2.3. Wearable applications

Identifying human motion and differentiation of various activities are crucial parameters for human-machine interactions [57], rehabilitation [58], and entertainment [59]. Numerous techniques have been developed to distinguish distinct human activities. The camera-implemented motion capture mode is frequently used, but it needs high power and can serve only in a certain domain [60]. On the contrary, inertial sensors can also distinguish different activities of humans, owing to the rigidity it has limitation in daily life applications [61]. However, the main limitation of these techniques is that they cannot enumerate the individual forces involved in each activity. To overcome



this limitation, flexible wearable sensors such as piezoelectric, piezoresistive, piezo capacitive, and triboelectric sensors were invented, which have potential applications in motion detection [9,23,62–64]. Furthermore, most human joints have multiple degrees of freedom and compose distinct forces, for instance, a wrist can have three different degrees of freedom: bending (different angles), stretching, and twisting [63]. In all cases, the force acting on the sensor varies, and hence based on the sensor performance, we can differentiate the activity. In this study,

EC10S+PNy 11 triboelectric sensor without a spacer (TES) was successfully demonstrated for real-time human motion detection. During the measurement, the sensor is initially connected to the piezo amplifier, the output of the amplifier is connected to the Biopac 150 system, and Biopac can transfer the data wirelessly to the system or mobile phone, which contains an acknowledgment software; the whole schematic representation is shown in Fig. 7(a). The Biopac system has 16 input channels; hence, it can detect 16 different activities (real-time) of

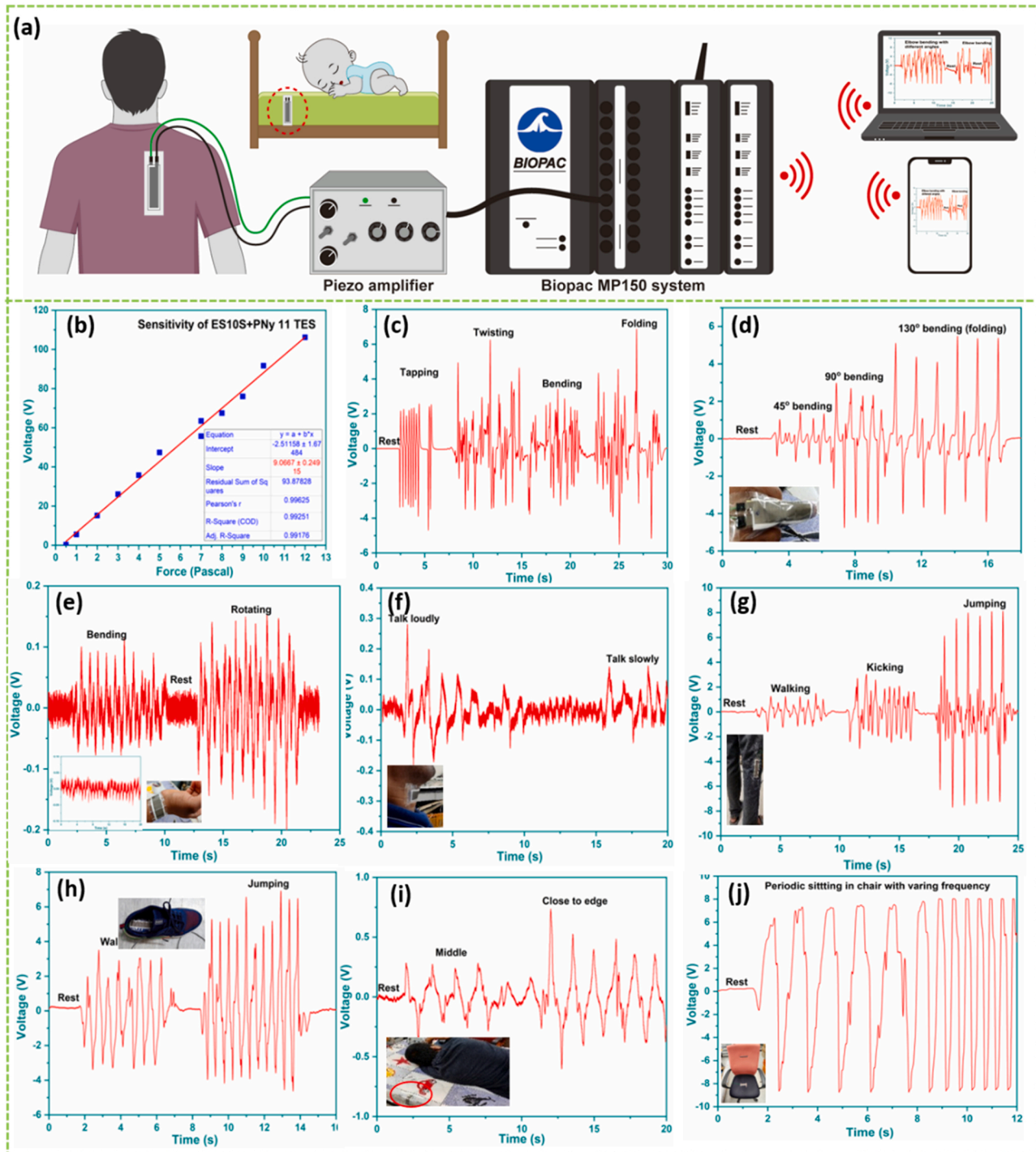


**Fig. 7.** (a) Schematic illustration of the experimental setup to measure human activities of EC10S+PNy 11 TES, (b) sensitivity of the sensor, (c) Sensing performance when the sensor experienced different physical deformations (tapping, twisting, bending, and folding), (d) and (e) detect and differentiate the different degrees of joint bending when the sensor is used as a finger ring and wrist band. (f) detects and differentiates the intensity of voice when the sensor is used as a neckband, (g) and (h) are the detection and differentiation of motion detection (walking, kicking and jumping) when the sensor placed on knee and shoe insole. (i) detect the sleeping position when the sensor placed on edge of the bed, (j) smart chair health care applications.

humans consecutively and can send them to readers. The EC10S+PNy 11 sensor identifies various human body motions when the sensor is placed on different body parts, such as the elbow, finger, shirt, wrist, pant, neck, and shoe insole. The sensor can also identify various motions generated from the bed and chair during human motions. Before testing the real-time wearable applications, the sensitivity of optimized EC10S+PNy 11 TES ( $2 \times 2 \text{ cm}^2$ ) is measured as a function of load (0.5–12.5 Pa) the values shown in [Supporting Information Fig. S12](#). The Voltage response of EC10S+PNy 11 TES with various forces is plotted in origin and fitted liner data as shown in [Fig. 7\(b\)](#). The linear fitting data (insert atable in [Fig. 7\(b\)](#)) shows a slope of  $9.01 \pm 0.2$ . The slope generally refers to the sensitivity of the sensor. Therefore, the sensitivity of the of EC10S+PNy 11 TES is 9 V/Pa. [Fig. 7\(c\)](#) shows the sensitivity of the EC10S+PNy 11 TES; the sensor can effectively sense finger tapping, twisting, bending, and folding (see [Fig. S4\(d-f\)](#) in the [Supporting Information](#)). When the sensor undergoes tapping it produces 4 V maximum, similarly 6 V for twisting, 2 V for bending, and 6.5 V for folding. From these results, we can observe that the TES shows a good response for twisting and folding rather than tapping, as shown in Video S3 in the Supporting Information. [Fig. 7\(d\)](#) shows the various bending angles of finer  $45^\circ$ ,  $90^\circ$ , and  $135^\circ$  will produce 1.8 V, 3.6 V, and 5.3 V, respectively when the sensor was used as a finger ring similar results were observed for elbow bending shown in [supplementary Information Fig. S13](#) (a) From these results, we can say that the as-prepared EC10S+PNy 11 TES can detect and differentiate different degrees freedom of joints. When the sensor is used as a wristband, it can differentiate the wrist bending (0.1 V) and rotation (0.15 V), here, rotation is generating more voltages than the bending shown in [Fig. 7\(e\)](#) and Video S3 in the Supporting Information. The wristband can also detect a pulse signal with extremely low voltages (0.002 V); however,  $\sim 6.5$  peaks every 5 s is equivalent to 78 peaks per minute, which is close to the average human pulse rate (72 bpm), as shown in inset [Fig. 7\(e\)](#). If the sensor is used as a neckband as shown in [Fig. 7\(f\)](#), it can detect and differentiate the intensity of voice, for instance, if a person voluntarily talks loudly, it records a high voltage (0.3 V), and if they talk slowly, it produces low voltages (0.1 V), therefore it has a potential application in voice detection. When the sensor was placed on the shirt (backside), pants (near the knee), and shoe insole, it could detect various human activities, such as walking, kicking, and jumping as well as differentiate them, as shown in [Fig. 7\(g\)](#) and (h) and [supporting Information Fig. S13](#) (b). For instance, if the sensor is placed on the knee it will generate different voltages for different activities such as for walking (2 V), kicking (2.7 V) and jumping (7.7 V) similar when the sensor placed on the shoe insole. However, the shoe insole generates fewer voltages (6 V) compared to the knee and back (8 V), this is because, in the beginning, the sensor shows a good response for twisting and folding rather than tapping, herein shoe insole case act tapping mechanism whereas other two as bending or folding. If the EC10S+PNy 11 triboelectric sensor is placed on a pocket, it can act as a smart pocket and prevent pickpocketing. When the sensor is placed on a pocket and someone inserts a hand in the pocket, it will generate some voltage (more than 1 V), as shown in [Supporting Information Fig. S13\(c\)](#). The real-time measurements are shown in Video S4 in the Supporting Information. Based on this, the theft can be caught by integrating with custom-made software in the future. Finally, the EC10S+PNy 11 TES can also be used in healthcare applications such as smart beds and smart chairs. For instance, if any kids or patients were lying on a bed containing a triboelectric sensor (on edge) as shown in Video S5. When the person is lying in the middle of the bed, the sensor shows a low voltage (0.4 V), whereas, during body movements (observing coma patients), such as when the person moves towards the edge, the sensor shows a high voltage of 0.7 V. These variations can be seen in [Fig. 7\(i\)](#) and Video S5 in the Supporting information. Based on these results, we can predict the fall and avoid damage using custom-designed software interfaces. Similarly, the sensors placed on seats can also detect irregular body moments, and periodic sitting can generate more than 8 V as shown in [Fig. 7\(j\)](#). This indicates that the

sensor has potential applications in continuous monitoring of the activities of drivers and paralysis patients. From the above results, it is clear that the ES10S+PNy 11 triboelectric sensor has potential applications in detecting and differentiating the various physical activities of humans continuously.

Supplementary material related to this article can be found online at [doi:10.1016/j.nanoen.2023.108178](https://doi.org/10.1016/j.nanoen.2023.108178).

#### 4. Conclusions

In this study, tribo-positive Nylon 11 films were successfully fabricated using the traditional electrospinning technique followed by facile PLL surface modification. The surface-modified Nylon electrospun membranes (PNy 11) showed higher TENG performance in terms of  $V_{OC}$ ,  $I_{SC}$ , and  $Q$ , that is, more than five times (from 26 to 137 V), four times (from  $0.8 \mu\text{A}$  to  $3.4 \mu\text{A}$ ), and three times (from 8.1 to 26 nC), respectively, than unmodified Nylon 11 electrospun (Ny 11) with an Ecoflex cast film (EC) frictional layer. This is because PLL offers more electron donating atoms N and O, which are instrumental in enhancing the positive polarity of Nylon 11. Further, the tribo-negativity of the Ecoflex films was enriched by incorporating different wt% (3–10) of the dielectric materials (MXene and  $\text{SrTiO}_3$ ). Among the different combinations, the synergistic effect of the surface modification of Nylon and 10 wt% (MXene and  $\text{SrTiO}_3$ )-embedded Ecoflex exhibits superior performance compared with others. Further, the output performance was evaluated as a function of external load, and the results suggest that the EC10M composite film was almost saturated when the external load increased from 2.5 N to 4.5 N. On the other hand, the EC10S composite film showed a linear relationship with the external pressure and achieved a maximum  $V_{OC}$  of 270 V and  $I_{SC}$  of  $7.2 \mu\text{A}$  at 12.5 N and 5 Hz frequency. The EC10S, and PNy 11 tribo-pair was optimized, and it showed a maximum power density of  $2 \text{ W/m}^2$ . The EC10S+PNy 11 TENG (with spacer) successfully powered low-power electronics (stopwatch) and lit up 111 LEDs, demonstrating its application as a force sensor. Similarly, the EC10S+PNy 11 TES (without spacer) was successfully used as a self-powered motion sensor (walking, running, and stretching), detecting different degrees of joint movements (elbow, finger, wrist, and knee); voice detecting sensor; and for health care applications (pulse detection, smart bed, and smart chair) to monitor real-time human activities. The EC10S+PNy 11 device has potential applications as energy harvesting and self-powered wearable sensors for real-time monitoring of human motion.

#### CRedit authorship contribution statement

**Gajula Prasad:** Conceptualization, Methodology, Investigation, Data curation, Formal analysis, Validation, Writing – original draft; **Sontyana Adonijah Graham:** Data curation, Formal analysis, Writing – review & editing; **Jae Su Yu:** Resources, Data curation, Validation, Writing – review & editing; **Hongdoo Kim:** Resources, Visualization, Validation, Writing – review & editing. **Dong-Weon Lee:** Resources, Funding acquisition, Validation, Supervision, Writing – review & editing.

#### Declaration of Competing Interest

The authors declare that they have no known competing financial interests or personal relationships that could have appeared to influence the work reported in this paper.

#### Data Availability

Data will be made available on request.

## Acknowledgments

This work was supported by the National Research Foundation of Korea (NRF) grant funded by the Korean government (MISIT) (2020R1A5A8018367).

## Appendix A. Supporting information

Supplementary data associated with this article can be found in the online version at [doi:10.1016/j.nanoen.2023.108178](https://doi.org/10.1016/j.nanoen.2023.108178).

## References

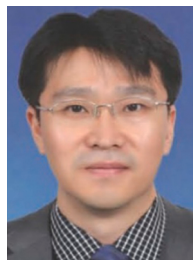
- [1] W. Gao, H. Ota, D. Kiriya, K. Take, A. Javey, Flexible electronics towards wearable sensing, *Acc. Chem. Res.* 52 (2019) 523–533.
- [2] M. Bariya, H.Y.Y. Nyein, A. Javey, Wearable sweat sensors, *Nat. Electron* 1 (2018) 160–171.
- [3] Y. Hattori, L. Falgout, W. Lee, S. Jung, E. Poon, J.W. Lee, I. Na, A. Geisler, D. Sadhwani, Y. Zhang, Y. Su, X. Wang, Z. Liu, Multifunctional skin-like electronics for quantitative, clinical monitoring of cutaneous wound healing, *Adv. Healthc. Mater.* 3 (2014) 1597–1607.
- [4] Y. Wang, L. Wang, T. Yang, X. Li, X. Zhang, M. Zhu, K. Wang, D. Wu, H. Zhu, Wearable and highly sensitive graphene strain sensors for human motion monitoring, *Adv. Funct. Mater.* 6 (2014) 4666–4670.
- [5] Y.C. Lai, J. Deng, S.L. Zhang, S. Niu, H. Guo, Z.L. Wang, Single-thread-based wearable and highly stretchable triboelectric nanogenerators and their applications in cloth-based self-powered human-interactive and biomedical sensing, *Adv. Funct. Mater.* 27 (2017), 1604462.
- [6] W. Song, X. Yin, D. Liu, W. Ma, M. Zhang, X. Li, P. Cheng, C. Zhang, J. Wang, Z. L. Wang, A highly elastic self-charging power system for simultaneously harvesting solar and mechanical energy, *Nano Energy* 65 (2019), 103997.
- [7] Q. Liu, X.X. Wang, W.Z. Song, H.J. Qiu, J. Zhang, Z. Fan, M. Yu, Y.Z. Long, Wireless single-electrode self-powered piezoelectric sensor for monitoring, *ACS Appl. Mater. Interfaces* 12 (2020) 8288–8295.
- [8] D.Y. Park, D.J. Joe, D.H. Kim, H. Park, J.H. Han, C.K. Jeong, H. Park, J.G. Park, B. Joung, K.J. Lee, Self-powered real-time arterial pulse monitoring using ultrathin epidermal piezoelectric sensors, *Adv. Mater.* 29 (2017), 1702308.
- [9] R.T. Selvan, Y.J. Ahn, K.J. Kim, H.D. Kim, Uniaxially drawn polylactic acid film based physiological sensor for monitoring sleeping parameters, *Fibers Polym.* 18 (2017) 1898–1905.
- [10] H. Xue, Q. Yang, D. Wang, W. Luo, W. Wang, M. Lin, D. Liang, Q. Luo, A wearable pyroelectric nanogenerator and self-powered breathing sensor, *Nano Energy* 38 (2017) 147–154.
- [11] B. Mahanty, S.K. Ghosh, K. Maity, K. Roy, S. Sarkar, D. Mandal, All-fiber pyro- and piezo-electric nanogenerator for IoT based self-powered health-care monitoring, *Mater. Adv.* 2 (2021) 4370–4379.
- [12] X. He, Y. Hao, M. He, X. Qin, L. Wang, J. Yu, Stretchable thermoelectric-based self-powered dual-parameter sensors with decoupled temperature and strain sensing, *ACS Appl. Mater. Interfaces* 13 (2021) 60498–60507.
- [13] M. Mukaida, K. Kirihara, S. Horike, Q. Wei, Stable organic thermoelectric devices for self-powered sensor applications, *J. Mater. Chem. A* 8 (2020) 22544–22556.
- [14] Y.C. Lai, H.W. Lu, H.M. Wu, D. Zhang, J. Yang, J. Ma, M. Shamsi, V. Vallem, M. D. Dickey, Elastic multifunctional liquid-metal fibers for harvesting mechanical and electromagnetic energy and as self-powered sensors, *Adv. Energy Mater.* 11 (2021), 2100411.
- [15] H. Oh, S.S. Kwak, B. Kim, E. Han, G.H. Lim, S.W. Kim, B. Lim, Highly conductive ferroelectric cellulose composite papers for efficient triboelectric nanogenerators, *Adv. Funct. Mater.* 29 (2019), 1904066.
- [16] W. Seung, M.K. Gupta, K.Y. Lee, K.S. Shin, J.H. Lee, T.Y. Kim, S. Kim, J. Lin, J. H. Kim, S.W. Kim, Nanopatterned textile-based wearable triboelectric nanogenerator, *ACS Nano* 9 (2015) 3501–3509.
- [17] T. Chen, Q. Shi, M. Zhu, T. He, L. Sun, L. Yang, C. Lee, Triboelectric self-powered wearable flexible patch as 3D motion control interface for robotic manipulator, *ACS Nano* 12 (2018) 11561–11571.
- [18] Y. Chen, Z. Deng, R. Ouyang, R. Zhang, Z. Jiang, H. Bai, H. Xue, 3D printed stretchable smart fibers and textiles for self-powered e-skin, *Nano Energy* 84 (2021), 105866.
- [19] G. Yao, L. Xu, X. Cheng, Y. Li, X. Huang, W. Guo, S. Liu, Z.L. Wang, H. Wu, Bioinspired triboelectric nanogenerators as self-powered electronic skin for robotic tactile sensing, *Adv. Funct. Mater.* 30 (2020), 1907312.
- [20] W. Ding, A.C. Wang, C. Wu, H. Guo, Z.L. Wang, Human-machine interfacing enabled by triboelectric nanogenerators and tribotronics, *Adv. Mater. Technol.* 4 (2019), 1800487.
- [21] K. Meng, S. Zhao, Y. Zhao, Y. Wu, S. Zhang, Q. He, X. Wang, Z. Zhou, W. Fan, X. Tan, J. Yang, J. Chen, A wireless textile-based sensor system for self-powered personalized health care, *Mater* 2 (2020) 896–907.
- [22] Z. Lin, X. Li, Z. Zhou, K. Meng, W. Wei, J. Yang, Z.L. Wang, Triboelectric nanogenerator enabled body sensor network for self-powered human heart-rate monitoring, *ACS Nano* 11 (2017) 8830–8837.
- [23] M.M. Fahad, M.S. Reza, G. Prasad, S.N. Jaisankar, K.J. Kim, H.D. Kim, Polysomnographic observation using triboelectric pressure sensor composed of polymer-pairs having coarse surface, *Fibers Polym.* 23 (2022) 1490–1499.
- [24] M. Ha, S. Lim, S. Cho, Y. Lee, S. Na, C. Baig, H. Ko, Skin-inspired hierarchical polymer architectures with gradient stiffness for spacer-free, ultrathin, and highly sensitive triboelectric sensors, *ACS Nano* 12 (2018) 3964–3974.
- [25] P. Bai, G. Zhu, Q. Jing, J. Yang, J. Chen, Y. Su, J. Ma, G. Zhang, Z.L. Wang, Membrane-based self-powered triboelectric sensors for pressure change detection and its uses in security surveillance and healthcare monitoring, *Adv. Funct. Mater.* 24 (2014) 5807–5813.
- [26] Z.L. Wang, J. Chen, L. Lin, Progress in triboelectric nanogenerators as a new energy technology and self-powered sensors, *Energy Environ. Sci.* 8 (2015) 2250–2282.
- [27] G. Zhu, J. Chen, T. Zhang, Q. Jing, Z.L. Wang, Radial-arrayed rotary electrification for high performance triboelectric generator, *Nat. Commun.* 5 (2014) 3426.
- [28] J. Chen, Z.L. Wang, Reviving vibration energy harvesting and self-powered sensing by a triboelectric nanogenerator, *Joule* 1 (2017) 480–521.
- [29] Q. Ling, X. Yan, X. Liao, Y. Zhang, Integrated multi-unit transparent triboelectric nanogenerator harvesting rain power for driving electronics, *Nano Energy* 25 (2016) 18–25.
- [30] L. Zhang, B. Zhang, J. Chen, L. Jin, W. Deng, J. Tang, H. Zhang, H. Pan, M. Zhu, W. Yang, Z.L. Wang, Lawn structured triboelectric nanogenerators for scavenging sweeping wind energy on rooftops, *Adv. Mater.* 28 (2016) 1650–1656.
- [31] D. Shindell, C.J. Smith, Climate and air-quality benefits of a realistic phase-out of fossil fuels, *Nature* 573 (2019) 408–411.
- [32] N. Zhang, C. Tao, X. Fan, J. Chen, Progress in triboelectric nanogenerators as self-powered smart sensors, *J. Mater. Res.* 32 (2017) 1628–1646.
- [33] M. Zhang, M. Zhao, M. Jian, C. Wang, A. Yu, Z. Yin, X. Liang, H. Wang, K. Xia, X. Liang, H. Wang, K. Xia, X. Liang, J. Zhai, Y. Zhang, Printable smart pattern for multifunctional energy-management e-textile, *Mater* 1 (2019) 168–179.
- [34] M. Kanik, M.G. Say, B. Daglar, A.F. Yavuz, M.H. Dolas, M.M.E. Ashry, M. Bayindir, A Motion- and Sound-Activated, 3D-Printed, chalcogenide-based triboelectric nanogenerator, *Adv. Mater.* 27 (2015) 2367–2376.
- [35] Y. Zhou, W. Deng, J. Xu, J. Chen, Engineering materials at the nanoscale for triboelectric nanogenerators, *Cell Rep. Phys. Sci.* 1 (2020), 100142.
- [36] Z. Lin, J. Yang, X. Li, Y. Wu, W. Wei, J. Liu, J. Chen, J. Yang, Large-scale and washable smart textiles based on triboelectric nanogenerator arrays for self-powered sleeping monitoring, *Adv. Funct. Mater.* 28 (2018), 1704112.
- [37] Z. Fang, K.H. Chen, X. Lu, C.F. Tan, G.W. Ho, Surface texturing and dielectric property tuning toward boosting of triboelectric nanogenerator performance, *J. Mater. Chem. A* 6 (2018) 52–57.
- [38] D. Kim, I.W. Tcho, I.K. Jin, S.J. Park, S.B. Jeon, W.G. Kim, H.S. Cho, H.S. Lee, S. C. Jeoung, Y.K. Choi, Direct-laser-patterned friction layer for the output enhancement of a triboelectric nanogenerator, *Nano Energy* 35 (2017) 379–386.
- [39] Z. Wang, L. Cheng, Y. Zheng, Y. Qin, Z.L. Wang, Enhancing the performance of triboelectric nanogenerator through prior-charge injection and its application on self-powered anticorrosion, *Nano Energy* 10 (2014) 37–43.
- [40] G.G. Cheng, S.K. Jiang, K. Li, Z.Q. Zhang, Y. Wang, N.Y. Yuan, J.N. Ding, W. Zhang, Effect of argon plasma treatment on the output performance of triboelectric nanogenerator, *Appl. Surf. Sci.* 412 (2017) 350–356.
- [41] J. Chen, H. Guo, X. He, C. Liu, Y. Xi, H. Shi, C. Hu, Enhancing performance of triboelectric nanogenerator by filling high dielectric nanoparticles into sponge PDMS film, *ACS Appl. Mater. Interfaces* 8 (2016) 736–744.
- [42] I.W. Park, J. Choi, K.Y. Kim, J. Jeong, D. Gwak, Y. Lee, Y.H. Ahn, Y.J. Choi, Y. J. Hong, W.J. Chung, M. Lee, K. Heo, Vertically aligned cyclo-phenylalanine peptide nanowire-based high-performance triboelectric energy generator, *Nano Energy* 57 (2019) 737–745.
- [43] W. Seung, M.K. Gupta, K.Y. Lee, K.S. Shin, J.H. Lee, T.Y. Kim, S. Kim, J. Lin, J. H. Kim, S.W. Kim, Nanopatterned textile-based wearable triboelectric nanogenerator, *ACS Nano* 9 (2015) 3501–3509.
- [44] G. Zhu, C. Pan, W. Guo, C.Y. Chen, Y. Zhou, R. Yu, Z.L. Wang, Triboelectric-generator-driven pulse electrodeposition for micropatterning, *Nano Lett.* 12 (2012) 4960–4965.
- [45] M. Salauddin, S.M.S. Rana, M. Sharifuzzaman, M.T. Rahaman, C. Park, H. Cho, P. Maharjan, T. Bhatta, J.Y. Park, A. Novel, mxene/ecoflex nanocomposite-coated fabric as a highly negative and stable friction layer for high-output triboelectric nanogenerators, *Adv. Energy Mater.* 11 (2021), 2002832.
- [46] C. Jiang, C. Wu, X. Li, Y. Yao, L. Lan, F. Zhao, Z. Ye, Y. Ying, J. Ping, All-electrospun flexible triboelectric nanogenerator based on metallic MXene nanosheets, *Nano Energy* 59 (2019) 268–276.
- [47] J.H. Kim, B.K. Jung, J.H. Jung, J.Y. Park, Enhanced triboelectrification of the polydimethylsiloxane surface by ultraviolet irradiation, *Appl. Phys. Lett.* 108 (2016), 133901.
- [48] H.J. Kim, J.H. Kim, K.W. Jun, J.H. Kim, W.C. Seung, O.H. Kwon, J.Y. Park, S. W. Kim, I.K. Oh, Silk nanofiber-networked bio-triboelectric generator: silk Bio-TEG, *Adv. Energy Mater.* 6 (2016), 1502329.
- [49] Y. Peng, L. Zheng, Y. Zhen, D. Wang, F. Zhou, W. Liu, Leaves based triboelectric nanogenerator (TENG) and TENG tree for wind energy harvesting, *Nano Energy* 55 (2019) 260–268.
- [50] Y. Liu, Y. Zheng, Z. Wu, L. Zheng, W. Sun, T. Li, D. Wang, F. Zhou, Conductive elastic sponge-based triboelectric nanogenerator (TENG) for effective random mechanical energy harvesting and ammonia sensing, *Nano Energy* 79 (2021), 105422.
- [51] H. Lee, H.E. Lee, S. Wang, S.M. Kang, D. Lee, Y.H. Kim, J.H. Shin, Y.W. Lim, K. J. Lee, B.S. Bae, Hierarchically surface-textured ultrastable hybrid film for large-scale triboelectric nanogenerators, *Adv. Funct. Mater.* 30 (2020), 2005610.
- [52] S. Chun, I.Y. Choi, W. Son, J. Jung, S. Lee, H.S. Kim, C. Pang, W. Park, J.K. Kim, High-output and bending-tolerant triboelectric nanogenerator based on an interlocked array of surface-functionalized indium tin oxide nanohelices, *ACS Energy Lett.* 4 (2019) 1748.



- [53] S.H. Shin, Y.H. Kwon, Y.H. Kim, J.Y. Jung, M.H. Lee, J. Nah, Triboelectric charging sequence induced by surface functionalization as a method to fabricate high performance triboelectric generators, *ACS Nano* 9 (2015) 4621–4627.
- [54] F.G. de A. Dias, A.G. Veiga, A. Pedro A. da C.P. Gomes, M.F. da Costa, M.Luiza M. Rocco, Using XPS and FTIR spectroscopies to investigate polyamide 11 degradation on aging flexible risers, *Polym. Degrad. Stab.* 195 (2022), 109787.
- [55] S.M.S. Rana, M.T. Rahman, M. Saladdin, S. Sharma, P. Maharjin, T. Bhatta, H. Cho, C. Park, J.Y. Park, Electrospun PVDF-TrFE/MXene nanofiber mat-based triboelectric nanogenerator for smart home appliances, *ACS Appl. Mater. Interfaces* 12 (2021) 4955.
- [56] X. Yang, W.A. Daoud, Synergetic effects in composite-based flexible hybrid medical energy harvesting generator, *J. Mater. Chem. A* 5 (2017) 9113–9121.
- [57] W.R. Harper, *Contact and frictional electrification*, Laplacian Press: *Morgan Hill*, Calif, 1998.
- [58] M. Zhu, Z. Sun, Z. Zhang, Q. Shi, T. He, H. Liu, T. Chen, C. Lee, Haptic-feedback smart glove as a creative human-machine interface (HMI) for virtual/augmented reality applications, *Sci. Adv.* 6 (2020) 1.
- [59] C.M. Boutry, Y. Kaizawa, B.C. Schroeder, A. Chortos, A. Legrand, Z. Wang, J. Chang, P. Fox, Z. Bao, A stretchable and biodegradable strain and pressure sensor for orthopaedic application, *Nat. Electron.* 1 (2018) 314–321.
- [60] K.K. Kim, I. Ha, M. Kim, J. Choi, P. Won, S. Jo, S.H. Ko, A deep-learned skin sensor decoding the epicentral human motions, *Nat. Commun.* 11 (2020) 1.
- [61] S. Misra, J. Singha, R.H. Laskar, Vision-based hand gesture recognition of alphabets, numbers, arithmetic operators and ASCII characters in order to develop a virtual text-entry interface system, *Neural Comput. Appl.* 29 (2018) 117–135.
- [62] S.Z. Homayounfar, T.L. Andrews, Wearable sensors for monitoring human motion: a review on mechanisms, materials, and challenges, *SLAS Technol.* 25 (2020) 9–24.
- [63] D. Sengupta, J. Romano, A.G.P. Kottapalli, Electrospun bundled carbon nanofibers for skin-inspired tactile sensing, proprioception and gesture tracking applications, *npj Flex. Electron* 5 (2021) 1.
- [64] L. Jin, Z. Li, Z. Liu, B. Richardson, Y. Zheng, L. Xu, Z. Chen, H. Zhai, H.D. Kim, Q. Song, P. Yue, S.Q. Xie, K.J. Kim, Y. Li, Flexible unimodal strain sensors for human motion detection and differentiation, *npj Flex. Electron* 6 (2022) 1.



**Sontyana Adonijah Graham** is currently pursuing his Ph.D. in Electronic Engineering under the supervision of Prof. Jae Su Yu. at Kyung Hee University, Republic of Korea. He received his Master's degree in Nanoscience and Nanotechnology (2017) at the National Center for Nanoscience and Nanotechnology, University of Madras, India. His research interest includes various energy harvesting applications, biocompatible and bioinspired electronics, and functional nanomaterials for electronics and biomedical applications.



**Jae Su Yu** received his Ph.D. degree in optoelectronic engineering from the Department of Information and Communications, Gwangju Institute of Science and Technology, Republic of Korea, in 2002. Afterward, he joined in Center for Quantum Devices, Northwestern University, Evanston, IL, as a Postdoctoral Fellow (2002). Since 2006, he has been a Tenured Professor in the Department of Electronic Engineering, Director of Institute for Wearable Convergence Electronics, Kyung Hee University, Republic of Korea. He has authored or co-authored more than 450 SCI(E) indexed journal papers. His recent research interests include supercapacitors, nanogenerators, solar cells, optical sensors, nanophotonics, and phosphors.



**Prof. Hongdoo Kim** is currently serving as Emeritus Professor at Kyung Hee University, Korea. He received his Ph. D degree in Physical Chemistry, from Univ. of Wisconsin-Madison, Wisconsin, USA. He worked as a Guest Scientist, in Polymer Division, NIST, USA. His research interests are Piezoelectric and Triboelectric Polymer Sensors, Polymer Blends, Thin films, and Nanotechnology. He specializes in the manufacturing of polymer-based Wearable sensors, Semiconductor Device Physics, and Organic Electronics.



**Prof. Dong-Weon Lee** received his Ph.D. degrees in Mechatronics Engineering from Tohoku University, Sendai, Japan in 2001. He has been a professor of Mechanical Engineering at Chonnam National University (CNU), Republic of Korea since 2004. Prior to joining the university, he mainly studied micro cantilever devices chemical AFM and high-density data storage applications at the IBM Zurich Research Laboratory in Switzerland. His research interests at CNU include smart cantilever devices, miniaturized energy harvester, smart structures & materials, and nanoscale transducers for biomedical applications. He was a member of the Technical Program Committee of IEEE MEMS conference, IEEE Sensors Conference, Transducers, and Microprocesses and Nanotechnology Conference etc.



**Dr. Gajula Prasad** is a postdoctoral researcher at the Chonnam National University, South Korea. He received his M.Sc. from Sri Venkateswara University, and his Ph.D. from the Vellore institute of technology (VIT) University, India. He has worked for 3 years as a postdoctoral researcher at the Guangdong University of Technology, China, and the Kyung Hee University, South Korea. His interests include Surface-modifications, Super-hydrophobic coatings, Piezoelectric and Triboelectric sensors, Electrodeposition, Electrospinning and HVOF coatings. He specializes in the manufacturing of polymer-based electrospun composite membranes and Wearable electronics.